Article:
Tokgoz, F., Zhu, Z.Q., Chen, X. et al. (2026) Novel hybrid magnet asymmetric rotors for electric vehicles. IEEE Transactions on Transportation Electrification. p. 1. ISSN: 2577-4212

https://doi.org/10.1109/tte.2026.3655667

Novel Hybrid Magnet Asymmetric Rotors for Electric Vehicles

Furkan Tokgoz, *Member, IEEE*, Z.Q. Zhu, *Fellow, IEEE*, Xiao Chen, *Senior Member, IEEE*, Han Yang, Lianghui Yang, and Chaohui Liu

***Abstract*—This paper proposes two novel hybrid magnet rotor topologies, spoke-V and spoke-delta, for interior permanent magnet synchronous machines (IPMSMs) for reducing rare-earth magnet usage while maintaining high electromagnetic performance in electric vehicles. Using the Tesla Model 3 IPMSM as a reference, the models are parametrized and multi-objective optimization is performed. The proposed spoke-V and spoke-delta configurations achieve NdFeB volume reductions of 19.4% and 25.8%, respectively, while matching the torque performance of the reference machine. This results in a 20.5% and 35.1% improvement in torque per unit volume of rare-earth material. Detailed electromagnetic analyses are conducted under open-circuit, peak-load, and torque-speed characteristic analysis under full operating conditions, demonstrating the feasibility of the proposed topologies for high-speed electric vehicle applications. A small-scale prototype is manufactured and tested to verify the accuracy of the calculations. These findings highlight the potential of asymmetric hybrid magnet rotor designs to deliver less rare-earth and high-performance IPMSMs, contributing to the development of more sustainable and cost-effective electric drive solutions.**

***Index Terms*—asymmetric, electric vehicles, ferrite, hybrid magnet, spoke.**

I. INTRODUCTION

INTERIOR permanent magnet synchronous machines (IPMSMs) have become the preferred choice for electric vehicle (EV) propulsion systems due to their high torque density, excellent efficiency, and wide speed operating range [1]-[2]. The torque production mechanism in IPMSMs arises from both permanent magnet (PM) excitation and saliency induced reluctance torque, allowing for effective torque control over a broad range of operating conditions [3]-[4].

Despite their performance advantages, conventional IPMSMs rely heavily on rare-earth materials, most notably neodymium-iron-boron (NdFeB) magnets, which are expensive and subject to significant geopolitical and environmental concerns [5]-[6]. The limited and geographically concentrated supply chain of rare-earth elements introduces risks to the sustainability and scalability of EV powertrains [7]-[8]. Consequently, there is a growing body of research focused on reducing or eliminating the use of rare-earth magnets in electric machines while maintaining high performance.

One approach involves replacing NdFeB magnets with ferrite magnets, which are more abundant, less expensive, and environmentally friendly [9]. However, ferrites suffer from lower remanence and coercivity, making them prone to demagnetization and limiting their effectiveness in high-torque, high-speed applications. To address these limitations, hybrid rotor topologies incorporating both ferrite and NdFeB magnets have been proposed [10]. These designs aim to leverage the high coercivity and flux density of NdFeB magnets while using ferrite magnets to reduce material cost and improve electromagnetic performance [11]-[12]. However, many of these studies focus on symmetrical rotor configurations, which do not fully exploit the potential benefits of flux alignment and torque enhancement achievable through rotor asymmetry.

Recent studies have demonstrated that asymmetric rotor topologies can alter the magnetic field distribution in a manner that enhances the alignment between the PM torque and reluctance torque vectors, thereby increasing the resultant electromagnetic torque even without changing the magnitude of the individual torque components [13]-[16]. This phenomenon, often referred to as the magnetic field shifting effect, is generated by deliberate geometric asymmetry in the rotor and allows for more effective utilization of the magnetic field, especially when the machine operates at optimized phase advance angles [17]-[18]. In literature, various asymmetric IPMSM designs have been proposed to reduce rare-earth PM volume while maintaining comparable torque performance [19]. Although rotor asymmetry is commonly introduced by modifying the geometry within a single pole, there are alternative approaches in which asymmetry is achieved by designing one rotor pole differently from the others [20]-[21].

An additional method for enhancing torque per unit volume of rare-earth magnet involves combining rotor asymmetry with the use of multiple magnet types, such as high energy density NdFeB and low cost ferrite magnets. This

This work is supported by Xiamen NEVC Advanced Electric Powertrain Technology Innovation Centre, P. R. China under Agreement No. HT0502-202203010928.

Furkan Tokgoz is with the University of Sheffield, and with Monumo, Cambridge, United Kingdom (e-mail: tokgozfurkan@gmail.com).

Zi-Qiang Zhu is with the Hong Kong Polytechnic University (e-mail: z.q.zhu@polyu.edu.hk).

Xiao Chen is with the University of Sheffield (e-mail: xiao.chen@sheffield.ac.uk).

Han Yang and Lianghui Yang are with Xiamen NEVC Advanced Electric Powertrain Technology Innovation Center, Xiamen 361026, China. (e-mail: yanghan@xiamen-nevc.com.cn, yanglianghui@xiamen-nevc.com.cn).

Chaohui Liu is with the National New Energy Vehicle Technology Innovation Center, Beijing 100176, China (e-mail: liuchaohui@nevc.com.cn).

hybrid approach allows further reduction of rare-earth material usage while maintaining or improving electromagnetic performance [22]-[23]. [24] uses AlNiCo and NdFeB magnets in combination with asymmetry for a memory machine. For instance, [25] demonstrates the use of a combined ferrite-NdFeB magnet structure to achieve this goal. Similarly, several studies have improved hybrid magnet asymmetric rotors by repositioning NdFeB magnets to induce beneficial asymmetry. These designs have not only increased torque output but also reduced torque ripple due to the smoothing effect of flux redistribution [27]. In [28], a mixed-magnet V-shaped rotor is proposed for EV applications, achieving a reported cost reduction of 21% while preserving performance requirements of a commercial EV powertrain.

Although a few studies have investigated asymmetric hybrid rotors for electric vehicle applications, their reported power density has generally remained limited. This gap highlights the need for further research into rotor topologies that can deliver both high electromagnetic performance and suitability for mass-production. This study introduces and evaluates two novel asymmetric hybrid rotor topologies, spoke-V and spoke-delta, aimed at reducing rare-earth magnet usage in high speed and high performance IPMSMs for electric vehicle applications. The designs are based on the machine geometry of the Tesla Model 3 IPMSM, which serves as the reference for both sizing and performance benchmarking. The proposed topologies utilize a series-parallel magnetic circuit of NdFeB and ferrite magnets to improve magnetic flux distribution and enhance resistance to demagnetization. A multi-objective optimization is performed using the non-dominated sorting genetic algorithm (NSGA-II) implemented within the ANSYS OptiSlang environment, with ANSYS Maxwell employed for finite element analysis (FEA). The optimized designs are evaluated under various operating conditions. Key performance aspects are analyzed in detail, and the results are validated using small scale prototype. The structure of the paper is as follows: Section II discusses the fundamental principles of asymmetric rotor design and the magnetic field shifting effect. Section III presents the proposed rotor topologies, their parametric definitions, and optimization methodology. Section IV details the FEA-based performance evaluation of the reference and proposed designs. Finally, Section V provides experimental validation results for a small-scale prototype of the spoke-V rotor.

II. Magnetic Field Shifting Principles

The electromagnetic torque generated by IPMSMs consists of two primary components: the reluctance torque, T_R, and the PM torque, T_{PM}, both in Nm. These torque components are directly influenced by the flux linkages in the direct (d) and quadrature (q) axes and can be analytically expressed using the machine's equivalent dq-axis model. For a rotor with symmetrical geometry, the flux linkages in the d and q axes, denoted as $\psi_{d,sym}$ and $\psi_{q,sym}$, can be written as

$$\psi_{d,sym} = \psi_{PM} - L_d i_s \sin(\beta) \quad (1)$$

$$\psi_{q,sym} = L_q i_s \cos(\beta) \quad (2)$$

where ψ_{PM} is the PM flux linkage in Wb, i_s is the stator current amplitude in A, β is the current phase advance angle in degrees, and L_d and L_q are the dq-axis inductances in H, respectively. In the case of a rotor with geometric asymmetry, the dq-axis flux linkages, denoted as $\psi_{d,asym}$ and $\psi_{q,asym}$, are altered due to the angular shift in the PM flux linkage vector. This shift is def ined by an angle γ in degrees, which represents the deviation of the PM flux linkage from the d-axis due to rotor asymmetry. The modified flux linkages are given by

$$\psi_d = \psi_{PM}\cos(\gamma) - L_d i_s \sin(\beta) \quad (3)$$

$$\psi_q = \psi_{PM}\sin(\gamma) + L_q i_s \cos(\beta) \quad (4)$$

This angular shift γ also results in a corresponding shift in the back-EMF waveform, as the PM flux linkage determines the phase of the induced voltage. The effect of this asymmetry is illustrated in Fig. 1, which shows the phasor diagrams of a machine with symmetrical and asymmetric rotor structures.

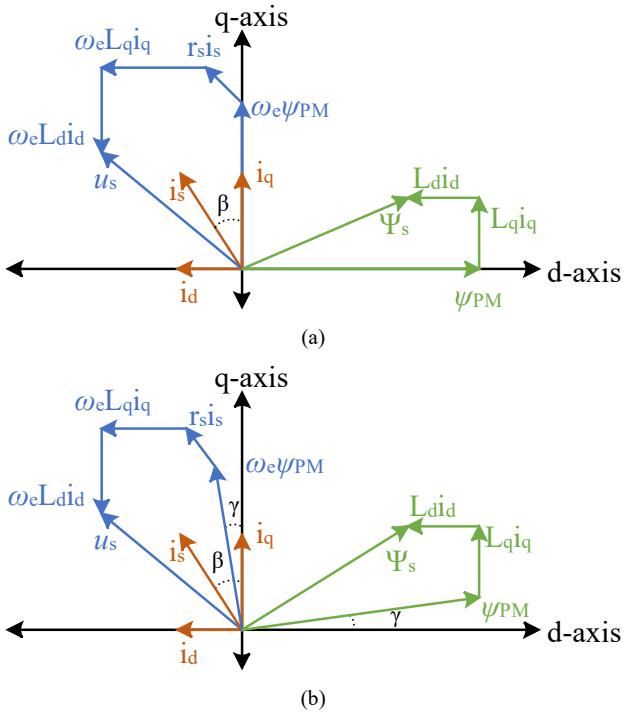

Fig. 1. Phasor diagrams of symmetrical and asymmetric PM machines. (a) Symmetrical, (b) Asymmetric.

Similarly, the dq axis voltages, u_d and u_q in V, are also altered and calculated by

$$u_d = R_s i_d + L_d \frac{d}{dt} i_d - \omega_e L_q i_q - \omega_e \psi_{PM} \sin(\gamma) \quad (5)$$

$$u_q = R_s i_q + L_q \frac{d}{dt} i_q + \omega_e L_d i_d + \omega_e \psi_{PM} \cos(\gamma) \quad (6)$$

where R_s is the phase resistance, i_d and i_q are the dq-axis currents, ω_e is the rotational speed, in rad/s. The PM torque

and the reluctance torque can be calculated for symmetrical machines by

$$T_{PM} = \frac{p}{2} m \psi_{PM} i_s \cos(\beta) \tag{7}$$

$$T_R = \frac{p}{4} m (L_q - L_d) {i_s}^2 \sin(2\beta) \tag{8}$$

where p is the number of pole pairs, m is the number of phases. For the asymmetric machines, the calculation of the torque-producing components can be done by

$$T_{PM} = \frac{p}{2} m \psi_{PM} i_s \cos(\beta - \gamma) \tag{9}$$

$$T_R = \frac{p}{4} m (L_q - L_d) {i_s}^2 \sin(2\beta) \tag{10}$$

Due to the angular shift γ introduced by the asymmetry in the rotor geometry, the alignment between the torque-producing components, PM torque and reluctance torque, is modified. In asymmetric rotor designs, the PM torque vector is no longer aligned along the *d*-axis but is instead shifted by the angle γ as shown in Fig. 2.

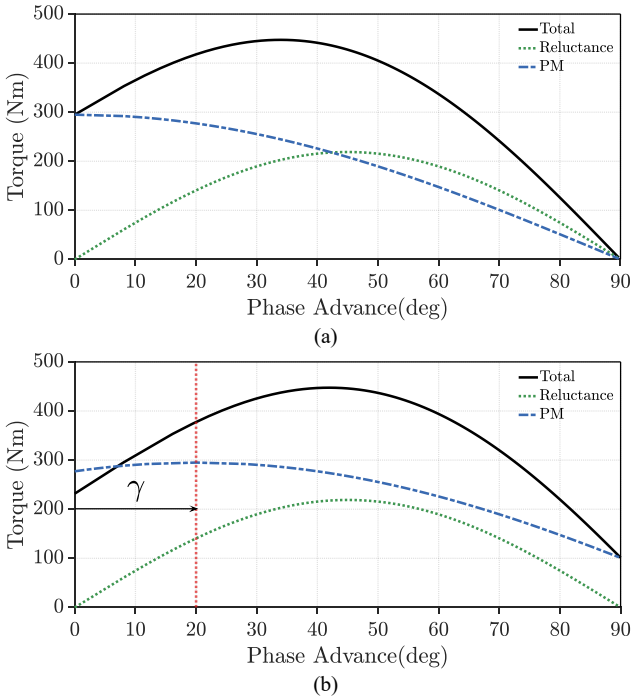

Fig. 2. Magnetic field shifting effect on asymmetric rotors. (a) Symmetrical, (b) Asymmetric.

Consequently, the optimal design strategy aims to minimize the angular separation between the PM torque vector and the reluctance torque vector, effectively aligning their directions to achieve higher torque addition as the output torque can be calculated by summation of these two torque components.

$$T_T = T_{PM} + T_R \tag{11}$$

where T_T is the synthetic torque. This alignment, facilitated by the magnetic field shifting effect, enables an increase in the total electromagnetic torque without altering the magnitudes of the individual PM or reluctance torque components. In other words, even if the PM and reluctance torques remain constant in magnitude, their improved phasor alignment results in a higher net torque output. This principle is particularly beneficial in the proposed asymmetric rotor designs, where maximizing the torque contribution from both sources is critical to improving torque density and reducing reliance on rare-earth materials.

III. Design of Asymmetric Rotors

In this study, the IPMSM used in the Tesla Model 3 is adopted as the reference design. This baseline machine features a 54-slot, 6-pole configuration and utilizes round wire windings with a fill factor of 0.4, representative of typical automotive manufacturing practices for round wire windings. The rotor has a single-layer V-shaped PM topology, using N52-grade neodymium magnets with a remanence of 1.44 T. To mitigate torque ripple in electromagnetic torque production, the rotor is designed with a three-step skew. A cross-sectional view of the reference motor geometry is presented in Fig. 3, while the principal geometric and electromagnetic parameters are listed in Table I. This machine serves as a reference for evaluating the performance of alternative topologies considered in this work, ensuring a realistic and relevant comparison.

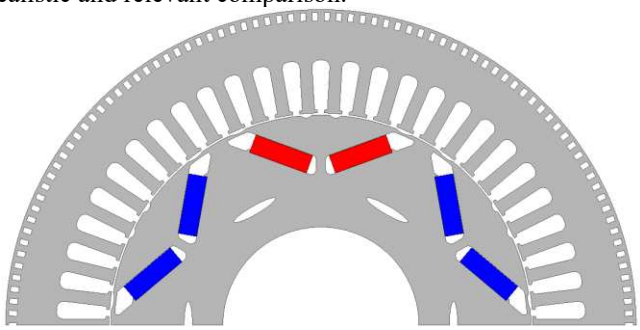

Fig. 3. Cross-section view of reference IPMSM design.

Table I Parameters of Reference Machine

Parameter	Value
Stator outer diameter (mm)	225
Stator inner diameter (mm)	151.3
Air gap (mm)	0.7
Rotor inner diameter (mm)	70
Lamination length (mm)	134
Stacking factor	0.95
Teeth width (mm)	4.75
Slot depth (mm)	17
End winding overhang (mm)	40
Number of parallel paths	3
Phase resistance at 20 C (mΩ)	4.75
Magnet dimensions - L-W-T (mm)	33×21×6.5
Angle of the V-shape (deg)	140
PM remanence (T)	1.44
Number of stator slots	54
Number of poles	6

A. *Parametrization of Hybrid Magnet Asymmetric Rotors*

The first machine that is designed is a hybrid V shaped rotor presented in [28]. However, one of the magnets has been replaced by the ferrite magnet to reduce the rare earth mineral usage. In order to have a fair comparison between the reference and the new designs the key dimensions are kept the same while the rotor and the stator are parametrized to be optimized. The parametrization of the model is given in Fig. 4.

The flux barriers of the hybrid V rotor design are shaped in polar coordinates with angles and radii. The ferrite flux barrier is defined using the angle of the first corner to the d-axis, θ_1. The radius of this corner is kept constant, and it is limited by the outer radius of the rotor and the bridge thickness which is assumed to be 1.5 mm for mechanical rigidity. Similarly, the outer corner of the NdFeB magnet is defined by θ_2 relative to the d-axis. Intersection of the outer edges of these two magnets are defined with the radius, r_F, and the angle, θ_3. This point can move radially and circumferentially to change the lengths of the magnets and the angle of the V-shape. The thicknesses of the magnets are defined with t_F and t_V. In order to make sure the feasibility of the designs, minimum circumferential distance between the edge of the rotor and the flux barriers are kept at 2 mm which may result in a tapered shape of the magnets as shown in the figure. In addition to these parameters, the split ratio of the machine which is the ratio of rotor diameter to stator outer diameter, is also made a variable. The stator is defined using the back-core length and the tooth thickness. Stranded round wires are used with copper fill factor equal to 40% of the slot area. The details of the stator parametrization are described in [3]. All designed machines use the same winding configuration for a fair comparison.

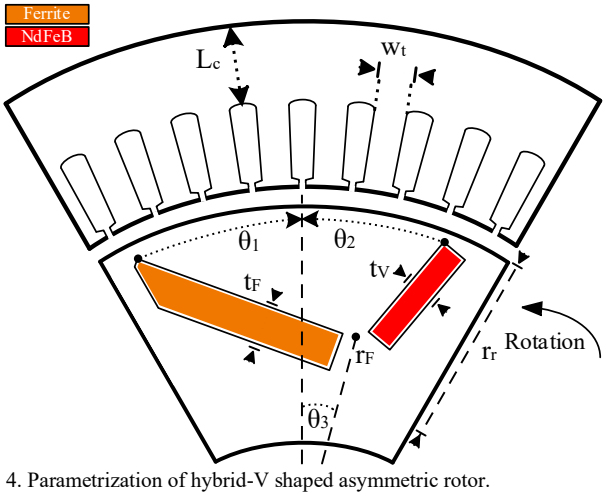

Fig. 4. Parametrization of hybrid-V shaped asymmetric rotor.

The first topology proposed in this paper is called spoke-V which is an asymmetric hybrid magnet rotor. The proposed structure can be seen in Fig. 5. In addition to the asymmetric hybrid magnet structure, the rotor has spoke NdFeB magnets added to counteract reduced flux density due to ferrite magnets. By increasing the number of layers, a higher output torque has been aimed. In addition to the design parameters listed for hybrid-V shaped rotor, spoke-V rotor has four more parameters to define spoke magnet and barrier. The width of the spoke barrier, w_S, the thickness of the magnet, t_S, the distances from the edges of the flux barriers to the magnets, d_1 and d_2, are additional parameters. Similar to the tapered ferrite magnet, the distance between two NdFeB magnets is also limited which may result in a tapered side magnet.

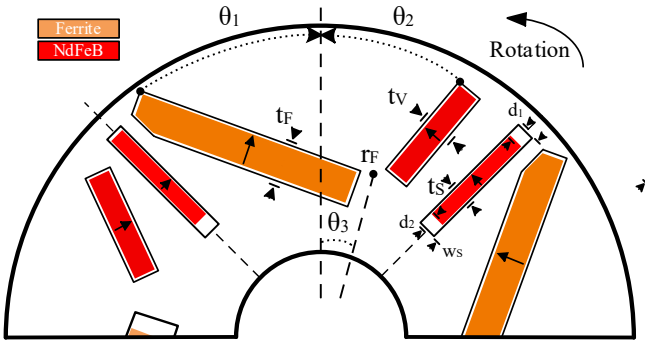

Fig. 5. Parametrization of spoke-V shaped asymmetric rotor.

The second motor topology, proposed in this paper is the spoke-delta design as given in Fig. 6. The design has another layer of NdFeB magnet in front of the ferrite magnet to achieve higher reluctance torque by increasing the number of layers. To define the new magnet and the flux barrier, five additional design parameters are used. The angle between the upper left corner of the flux barrier and d-axis, θ_4, the yaw angle of the magnet, θ_5, the thickness of the magnet, t_T, the width of the flux barrier, w_T, and the distance between the edges of the flux barriers and the magnet, d_3.

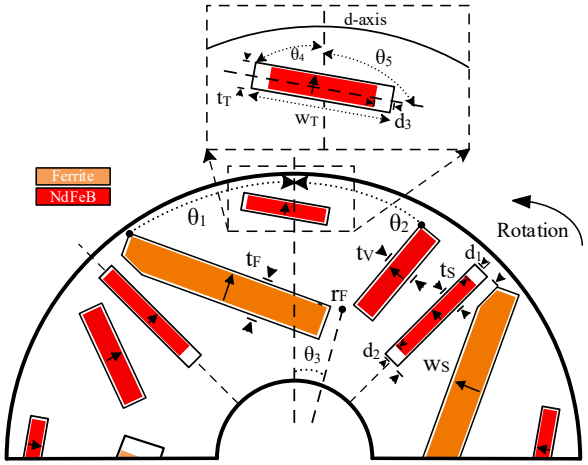

Fig. 6. Parametrization of spoke-delta shaped asymmetric rotor.

B. *Optimization Results*

The proposed machine topologies are modeled in ANSYS Maxwell based on the design variables outlined in the previous section. These models are integrated with ANSYS OptiSlang, which serves as the optimization framework and process controller. NSGA-II is used to carry out multi-

objective optimization. The objective functions are defined as maximizing the output torque and minimizing the volume of NdFeB magnets, given their high-cost relative to other materials commonly used in electrical machines. The upper and lower bounds of the design variables are presented in Table II. It is important to note that this table includes all variables used in the optimization of the spoke-delta machine. For the other machine topologies, only the relevant subset of variables corresponding to their specific parametrization is applied. Overall, it is found that the thicknesses and widths of the rare earth and ferrite magnets are the most effective design variables as they change the PM flux linkage and the saliency of the rotor. In this study, the asymmetry angle, γ, is not predefined but instead treated as a design variable within the optimization process to identify its optimum value. A controlled parametric study of γ will be considered in future work to provide further insights.

TABLE II DESIGN VARIABLES OF ASYMMETRIC HYBRID ROTORS

Variables	Lower Limit	Upper Limit
Radius of ferrite's inner corner, r_F (mm)	35	50
Thickness of ferrite, t_F (mm)	10	20
Thickness of spoke, t_S (mm)	1	7
Thickness of top magnet, t_T (mm)	1	9
Thickness of side magnet, t_V (mm)	1	7
Angle of ferrite's corner, θ_1 (deg)	20	30
Angle of side magnet's corner, θ_2 (deg)	10	25
Angle of middle point, θ_3 (deg)	-10	10
Angle of top magnet's corner, θ_4 (deg)	-5	5
Yaw angle of top magnet, θ_5 (deg)	-5	5
Distance from edge of flux barrier, d_1 (mm)	0	5
Distance from edge of flux barrier, d_2 (mm)	0	5
Distance from edge of flux barrier, d_3 (mm)	0	5
Width of spoke magnet's flux barrier, w_S (mm)	20	35
Width of top magnet's flux barrier, w_T (mm)	20	50
Tooth width, t_m (mm)	3	4.75
Back-core length (mm)	10	35
Split ratio	0.6	0.7
Phase advance angle (deg)	35	55

The design constraints and constants applied during the optimization process are summarized in Table III. Key sizing parameters, including the stator outer diameter, axial length, and rotor inner diameter, are fixed to match those of the reference IPMSM. The upper bounds for phase current and copper loss are used to account for the limitations of the inverter and thermal management system, respectively. The same N52-grade NdFeB magnets used in reference machine are utilized in all designs, while Y33H-grade ferrite magnets are selected as the cost-effective magnetic material for the ferrite magnet. M270-35A electrical steel is used across all configurations to maintain alignment with the baseline design.

TABLE III DESIGN CONSTANTS AND LIMITS OF OPTIMIZATION

Parameters	Value
Stator outer diameter (mm)	225
Rotor inner diameter (mm)	70
Axial length (mm)	134
Number of stator slots	54
Slot opening width (mm)	2.5
Airgap (mm)	0.7
Iron bridge thickness (mm)	1.5
Phase current (A)	<1100
Copper loss (kW)	<20
Current density (A/mm^2)	37
Fill factor	0.4

The multi-objective NSGA-II algorithm is configured with 50 generations and a population size of 100, resulting in a total of 5000 FEA evaluations. The population size is selected to provide a balance between achieving reliable convergence and maintaining a reasonable computational cost, as excessively large populations are found to increase in runtime without significant improvement in the quality of the Pareto front. The first constraint limits the torque ripple to below 5% to ensure smooth torque output, similar to that of the reference. The second enforces a minimum distance of 3 mm between the ferrite and spoke magnets, maintaining adequate center bridge thickness for mechanical robustness. Additional constraints, which are imposed in the optimization process, limit the number of feasible designs but they also ensure a fair comparison between the reference and optimized machines. These constraints included practical design boundaries which reflect realistic operating conditions. By applying these limits, optimization avoided impractical solutions and enabled an objective assessment of the proposed topologies against the baseline design.

The resulting Pareto frontiers are shown in Fig. 7, where the results for each topology are individually presented and subsequently compared with the reference design. The results show that the hybrid V-shaped rotor cannot meet the required output torque and was therefore excluded from further investigation. In contrast, the proposed spoke-V and spoke-delta rotor configurations produced optimal designs, delivering higher torque output while requiring a smaller volume of rare-earth permanent magnets.

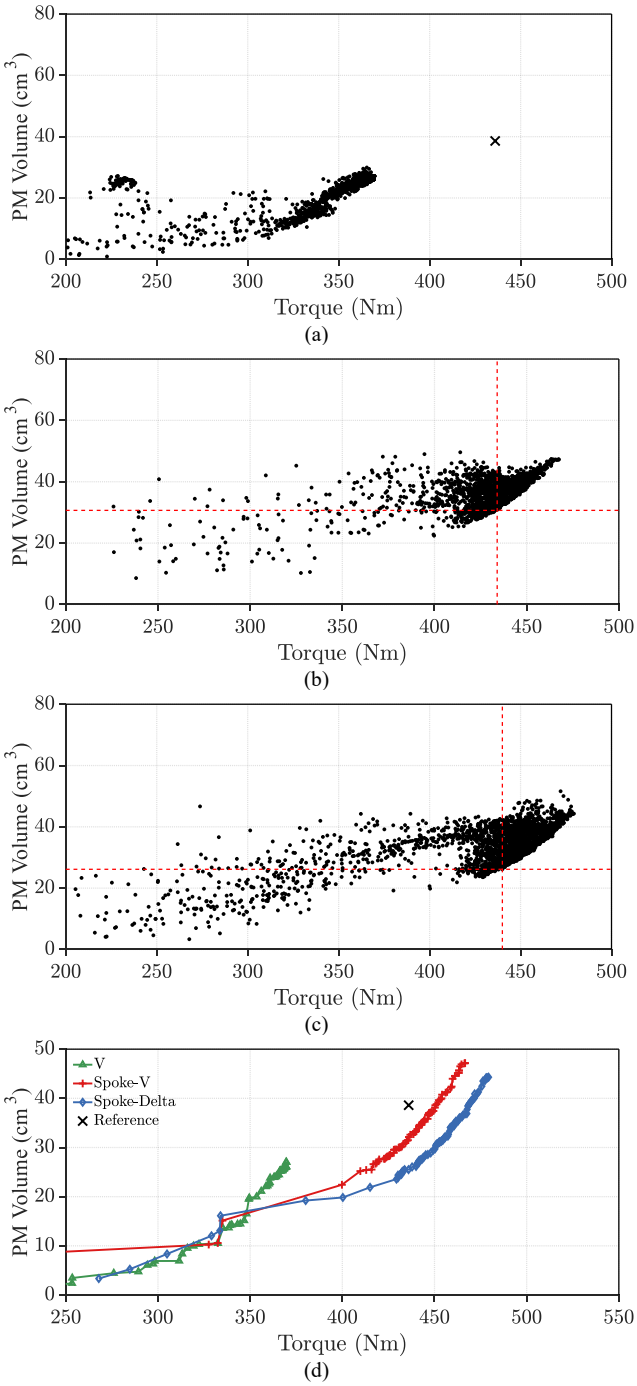

Fig. 7. Resultant Pareto frontiers. (a) Hybrid V, (b) Spoke-V, (c) Spoke-Delta, (d) Comparison of Pareto frontiers.

To examine the repeatability of the optimization process, the spoke-delta design was re-optimized under the same design variables and constraints. The resulting Pareto frontiers from the two independent runs are compared in Fig. 8. The close agreement between the two frontiers demonstrates the consistency and repeatability of the proposed optimization approach.

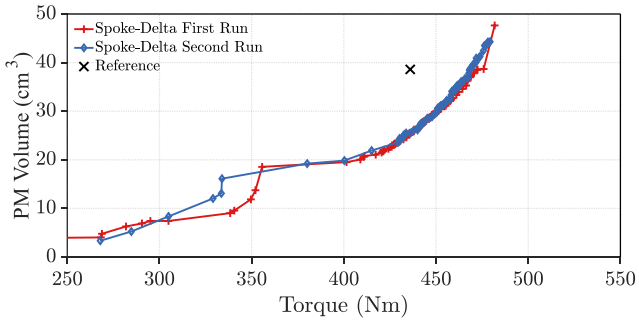

Fig. 8. Repeatability of the optimization of Spoke-Delta design.

For each of these two configurations, the design that minimizes rare-earth magnet volume while matching the reference machine's output torque is selected for further evaluation. The cross-sectional views of the selected rotor topologies are also shown in Fig. 9.

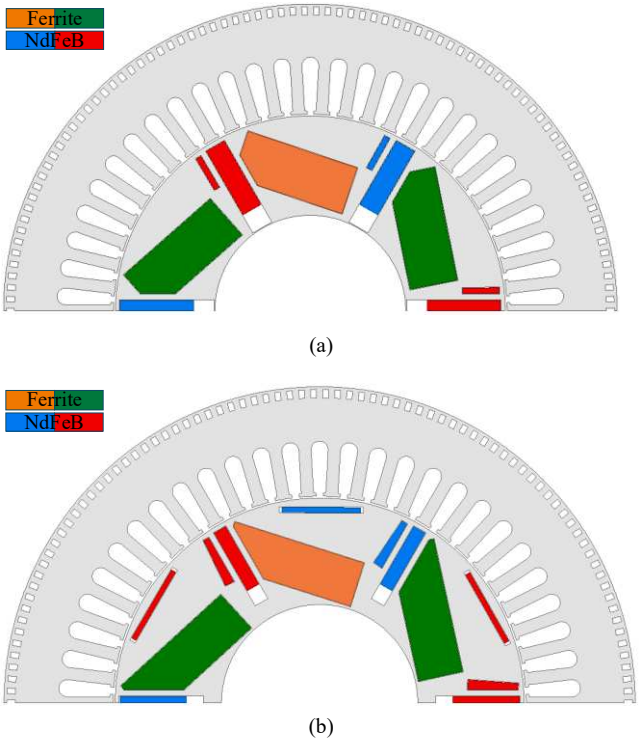

Fig. 9. Cross section view of chosen optimum asymmetric rotors. (a) Spoke-V, (b) Spoke-Delta.

IV. Finite Element Analysis Results

The optimized rotor topologies, along with the reference design, are evaluated using ANSYS Maxwell under a range of operating conditions to assess their electromagnetic performance. This section presents a detailed comparison of the proposed designs in terms of key performance indicators, including torque production, torque ripples, and flux distribution. To ensure a consistent and fair comparison, the same three-step rotor skewing technique employed in the reference is also applied to all optimized designs. Rotor skewing is known to mitigate torque ripple and reduce cogging torque by distributing the magnetic interaction over a wider angular range. By incorporating this feature into the newly designed models, the influence of rotor geometry on

overall performance can be isolated and accurately assessed.

A. Open Circuit Condition

The initial evaluation of the machine designs is conducted under open-circuit conditions to analyze the magnetic flux distribution within the rotor and stator. The resulting flux density distributions for each design are illustrated in Fig. 10. The simulation results reveal that the ferrite and spoke-mounted NdFeB magnets in the proposed rotor topologies form a combined series-parallel magnetic configuration. Specifically, the upper region of the NdFeB spoke magnet operates magnetically in series with the adjacent ferrite magnet, while the lower region functions in parallel. This hybrid magnetic coupling effectively enhances the magnetic loading in the airgap while simultaneously improving the demagnetization withstand capability of the ferrite magnets. Ferrite magnets, due to their inherently low coercivity, are more susceptible to demagnetization under adverse field conditions. However, the series-parallel arrangement with high coercivity NdFeB magnets helps maintain sufficient magnetic field strength across the ferrite segments, thereby stabilizing their performance and reducing the risk of partial or complete demagnetization. This configuration is particularly beneficial during high-load or flux-weakening operations where negative *d*-axis currents can impose significant reverse magnetizing fields.

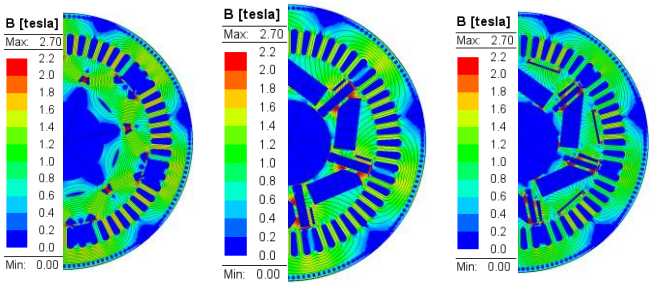

Fig. 10. Open circuit flux density distribution of machines. (a) Reference, (b) Spoke-V, (c) Spoke-Delta.

The radial flux density distributions within the air-gap region are computed and presented in Fig. 11. The results indicate that the spoke-V rotor configuration exhibits a higher fundamental component of the air-gap flux density compared to the other designs. In contrast, the spoke-delta topology demonstrates a reduction in the fundamental flux component. This reduction is primarily attributed to the introduction of the additional top layer of magnet in the spoke-delta configuration. This layer increases the magnetic reluctance along the *d*-axis, thereby diminishing the overall PM flux linkage. To further analyze this effect, the flux linkage waveforms and their corresponding spectral components are shown in Fig. 12. The harmonic spectrum confirms the reduction in the fundamental component for the spoke-delta design.

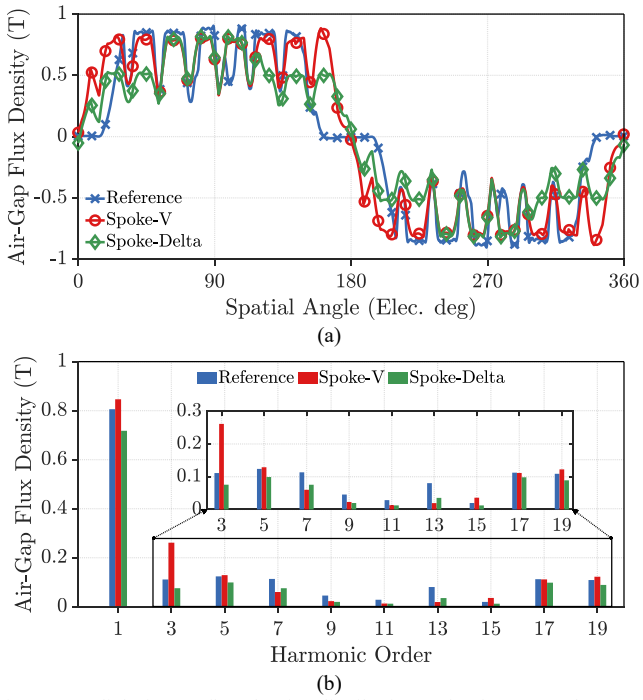

Fig. 11. Radial air-gap flux density distributions of reference and proposed models. (a) Waveforms, (b) Spectra.

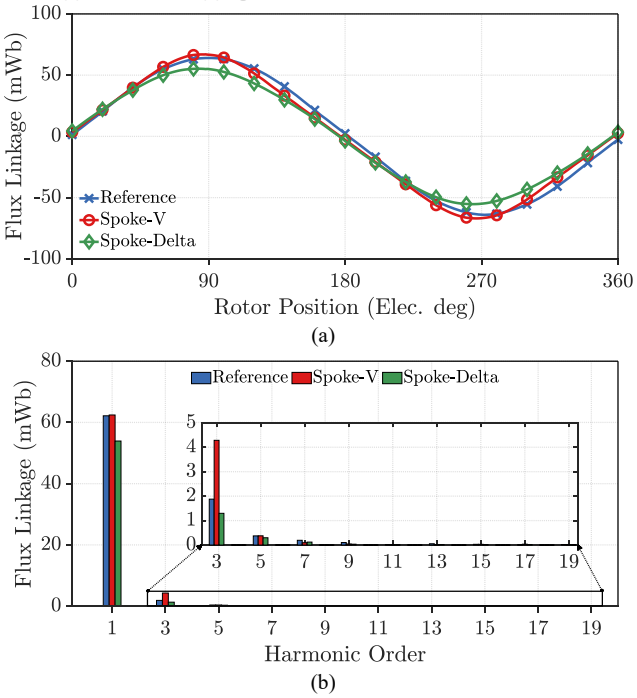

Fig. 12. Flux linkages of reference and proposed models. (a) Waveforms, (b) Spectra.

The back-EMF is directly related to the flux linkage in the machine windings and serves as a key indicator of the machine's electromagnetic performance. The back-EMF waveforms and their corresponding frequency spectra at a rotational speed of 5000 r/min are presented in Fig. 13. The results show that the fundamental component of the back-EMF in the spoke-delta rotor is reduced by approximately 14.3% compared to the reference design. This reduction is consistent with the observed decrease in flux linkage, primarily due to the increased *d*-axis reluctance introduced by

the upper magnet layer in the spoke-delta configuration. Conversely, the spoke-V rotor achieves a fundamental back-EMF magnitude comparable to that of the reference design, while exhibiting a significantly higher amplitude of the third-harmonic component. The presence of a stronger third harmonic reshapes the phase back-EMF waveform towards a more trapezoidal profile, which in turn enhances the effective magnitude of the fundamental component. This waveform shaping effect arises from the flux concentration and spatial distribution imposed by the spoke-V magnet arrangement, where the interaction of the magnet orientation and iron bridges produces a non-sinusoidal air-gap flux. Consistently, the radial air-gap flux density waveform, which is shown in Fig. 11, also reflects this characteristic, showing increased harmonic distortion but simultaneously reinforcing the average fundamental flux density. It is worth noting that the third-harmonic does not exist in the line back-EMF.

There is no significant change in the harmonic distortion of the back-EMF waveform with the introduction of asymmetric rotor designs. This indicates that the proposed asymmetry does not adversely affect the quality of the induced voltage.

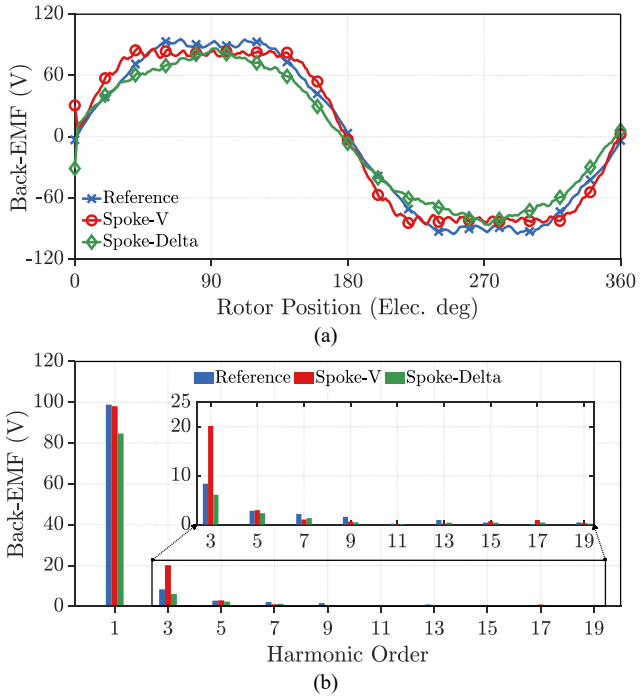

Fig. 13. Back-EMFs of reference and proposed models at 5000 r/min. (a) Waveforms, (b) Spectra.

B. Peak Load Condition

Further evaluations are conducted under peak load conditions, defined by the maximum achievable torque and the corresponding optimal phase advance angle at a rotational speed of 5000 r/min. The flux density distributions under these conditions are illustrated in Fig. 14, and a summary of the performance metrics is provided in Table IV. The spoke-delta design shows a slightly lower phase current than the other two machines because its phase resistance is marginally higher. In this comparison, the total copper loss is held constant. The efficiency calculation includes copper and core losses, while PWM-related and magnet losses are not taken into account. The simulation results demonstrate that both the proposed spoke-V and spoke-delta rotor topologies are capable of achieving electromagnetic performance comparable to the reference machine, while utilizing significantly less rare-earth PM material. Specifically, the spoke-V and spoke-delta configurations reduce the NdFeB magnet volume by 19.4% and 25.8%, respectively. As a result, the torque per unit volume of rare-earth magnet is improved by 20.5% in the spoke-V design and by 35.1% in the spoke-delta design, relative to the reference machine. The spoke-delta rotor exhibits higher magnetic saliency, which enhances the reluctance torque component while slightly reducing the contribution from the PM torque. This increased reliance on reluctance torque is beneficial for reducing rare-earth material usage without compromising overall torque output. Additionally, the asymmetry inherent in the rotor geometries further contributes to performance enhancement. By shifting the reluctance and PM torques of the machines higher output torque can be achieved with lower PM volume. These findings highlight the effectiveness of the proposed rotor topologies in reducing dependency on rare-earth materials while maintaining or enhancing torque performance, thereby contributing to more cost-effective electric machine designs.

Overall magnet rare earth magnet weight of the reference is 1.71 kg while it is 1.4 and 1.27 kg for the spoke-V and spoke-Delta design, respectively. Torque and power densities of the designs are not changed as the machine dimensions such as the outer diameter and the axial length are kept the same for fair comparison.

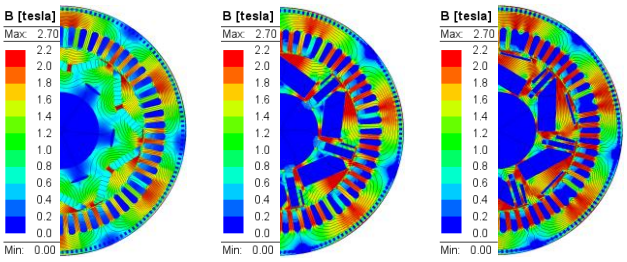

Fig. 14. On-load flux density distributions of machines. (a) Reference, (b) Spoke-V, (c) Spoke-Delta.

TABLE IV FEA RESULTS OF MACHINES WITH AND WITHOUT FERRITE

Parameter	Reference	Spoke-V	Spoke-Delta
Output power (kW)	228	227	231
Output torque (Nm)	436	436	441
Torque ripple (Nm/%)	16/3.7	12.7/2.9	13.7/3.1
Phase current (A)	1100	1100	1063
Phase advance angle (deg)	54	45	54
Saliency	1.42	1.28	1.76
Fundamental back-EMF (V)	98.7	98.1	84.72
RE magnet volume (cm^3)	37.6	30.7 (-19.4)	27.92 (-25.8%)
Torque per RE volume (Nm/ cm^3)	11.7	14.1 (20.5%)	15.8 (35.1%)
Core losses (kW)	0.87	0.84	0.82
Copper losses (kW)	20	20	20
Efficiency (%)	91.7	91.7	91.8

The resulting torque waveforms and their corresponding frequency spectra are shown in Fig. 15. The proposed designs achieve a comparable average output torque to the reference machine while exhibiting approximately 20% lower torque ripple. This improvement is primarily attributed to the attenuation of the 6th harmonic component in the torque spectrum. This reduction in the 6th harmonic is particularly important, as in the baseline machine the 6th harmonic showed a dominant component of the torque ripple. By suppressing this harmonic, the overall torque ripple is reduced, which leads to smoother electromagnetic performance, reduced mechanical vibration. Fig. 16 illustrates the variation of average output torque as a function of phase current and per created copper loss. The performance trends are largely consistent across all designs, demonstrating similar torque-current and torque-copper loss characteristics. The proposed rotor topologies attain this level of performance with a reduced volume of rare-earth permanent magnets. This shows the efficiency of magnetic circuit design, and the enhanced material utilization achieved through the integration of ferrite and NdFeB magnets in optimized geometries.

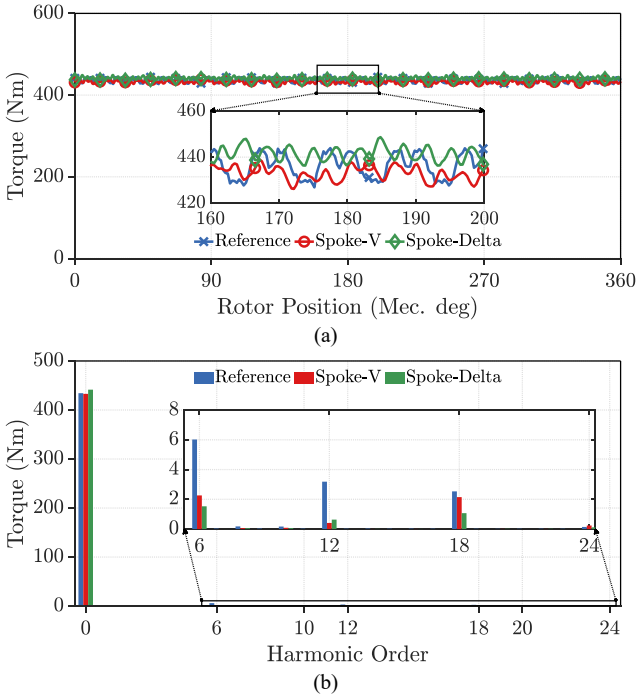

Fig. 15. Output torques at peak load conditions at 5000 r/min. (a) Waveforms, (b) Spectra.

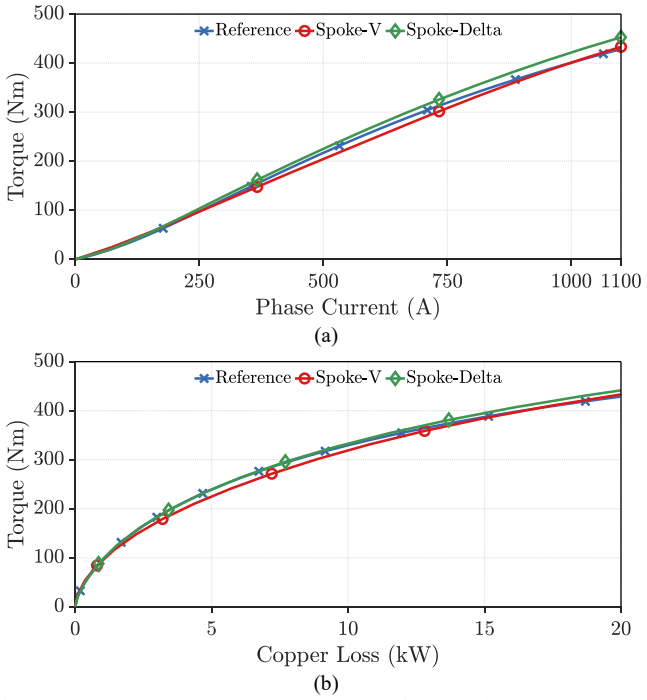

Fig. 16. Average output torque vs current and copper loss. (a) Torque per current, (b) Torque per copper loss.

The variations of average output torque with respect to the phase advance angle are illustrated in Fig. 17. The results indicate a noticeable shift in the optimal phase advance angle among the different rotor topologies. Specifically, the spoke-V configuration achieves its maximum torque at a phase advance angle of approximately 45°, whereas the spoke-delta configuration reaches its peak torque around 56°. This difference is primarily attributed to the higher magnetic saliency exhibited by the spoke-delta rotor. Increased saliency enhances the contribution of reluctance torque, thereby shifting the overall torque-angle characteristic towards higher phase advance angles. The observed rightward shift in the torque curve reflects the increased reliance on reluctance torque in the spoke-delta design, which complements the reduced PM flux linkage resulting from its geometry. These findings show the influence of rotor topology on optimal operating conditions and torque generation mechanisms. Understanding these shifts is essential for effective control strategy development, particularly in flux-weakening and high-speed operating regions where phase advance plays a critical role in maximizing performance.

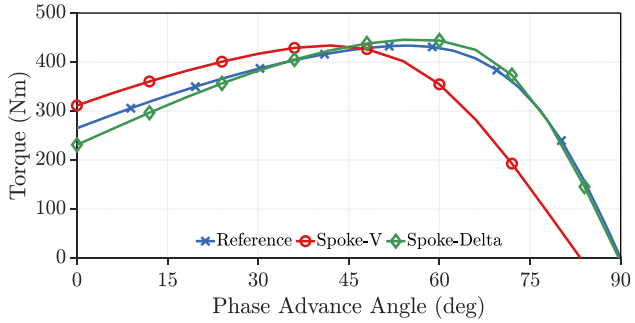

Fig. 17. Average output torque vs phase advance angle.

PWM losses are also examined to quantify their influence on the proposed machine designs. A switching frequency of 10 kHz is adopted, reflecting typical values in electric vehicle inverters. For a six-pole machine operating at 5000 r/min, the corresponding fundamental electrical frequency is 250 Hz. The DC-link voltage is set to 350 V, consistent with the reference operating conditions. Phase currents are obtained from the phase resistance, inductance, and back-EMF characteristics.

$$V_{AN} - R_S I_{AN} - e_{AN} = L_s \frac{dI_{AN}}{dt} \quad (12)$$

where V_{AN} is the phase voltage, R_S is the phase resistance, I_{AN} is the phase current, e_{AN} is the back-EMF obtained through FEA, and L_s is the phase inductance. The circuit parameters used for the calculations are listed in Table V. The phase current waveforms and corresponding spectra for the designed machines are shown in Fig. 18. Harmonic components at the 10 kHz switching frequency, as well as its multiples, are clearly visible. The magnitudes of these higher-order harmonics are similar across the designs. The phase currents including PWM induced harmonics are applied to the finite element model to estimate the associated losses.

TABLE V. CIRCUIT PARAMETERS OF MACHINES.

Parameter	Reference	Spoke-V	Spoke-Delta
Phase resistance (mΩ)	5.51	5.51	5.99
Phase inductance (μH)	79.8	75.2	71.3
RMS phase current (A)	1100	1100	1063

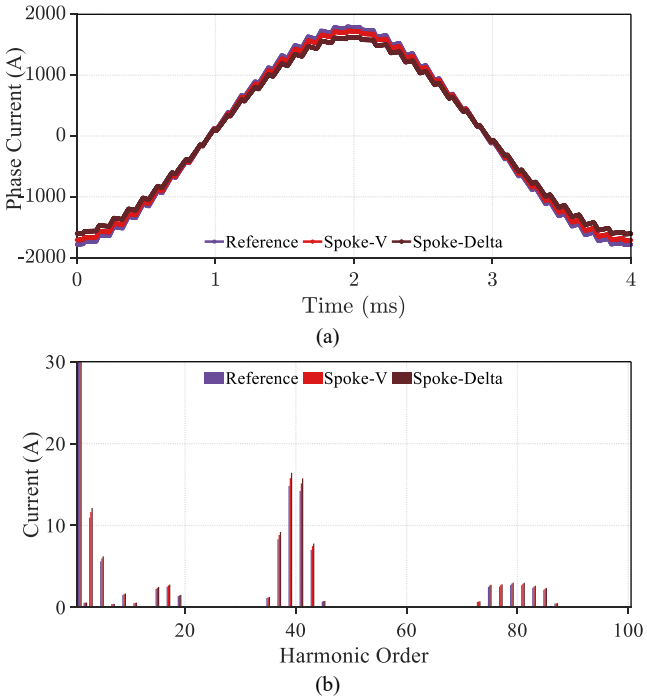

Fig. 18. Phase current waveforms of the machines at 10 kHz switching frequency. (a) Waveforms, (b) Spectra.

The resistivities of the ferrite and NdFeB magnets are assumed to be 100 Ω.m and 1.5 10^{-6} Ω.m, respectively. To evaluate the influence of PWM harmonics, the model resolution is increased by refining the mesh and reducing the time step to capture loss components around 10 kHz. The resulting losses, both with and without PWM-induced harmonics, are summarized in Table VI. The results show that the proposed designs have lower total magnet losses than the reference design. The reduction in PWM losses can be explained by reduction in NdFeB magnet volume in the proposed topologies. The ferrite magnets have roughly eight orders of magnitude higher electrical resistivity than the NdFeB magnets, which makes them a good electrical insulator. Reduced NdFeB volume also reduces the magnet losses on these magnets.

TABLE VI. EFFECT OF PWM HARMONICS ON MAGNET LOSSES.

Parameter	Reference		Spoke-V		Spoke-Delta	
	Sin.	PWM	Sin.	PWM	Sin.	PWM
Magnet loss (W)	42	76	34	62	32	57

A demagnetization analysis is performed for each machine topology under the extreme operating conditions to evaluate the robustness of both rare-earth and ferrite magnets during fault scenarios. Specifically, the machines are analyzed under short-circuit conditions by applying a *d*-axis current equal to twice the nominal maximum value, representing a worst-case scenario for demagnetization risk. The thermal operating limits of the magnets are also considered. The NdFeB magnets are assumed to operate at 120 °C, which significantly reduces their coercivity, while the ferrite magnets are evaluated at -20 °C. The results, presented in Fig. 19, confirm that no significant demagnetization occurs in either magnet type under these extreme conditions. This resilience is primarily attributed to the series-parallel magnetic configuration established between the spoke-mounted NdFeB and the ferrite magnets. In this arrangement, the high-coercivity NdFeB magnets support the ferrite magnets by maintaining a sufficient magnetizing field, thereby mitigating the risk of partial or full demagnetization. This interaction is important for preserving the magnetic integrity of the ferrite material, which is more vulnerable to demagnetizing fields.

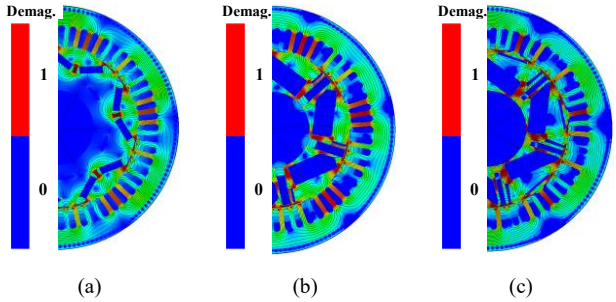

Fig. 19. Demagnetization performance of machines. (a) Reference, (b) Spoke-V, (c) Spoke-Delta.

The mechanical validation of both machines has also been done to check the validity of the proposed machine. The mechanical simulation is evaluated at 1.2 times overspeed

conditions according to IEC60034-1 and IEC60349-2. The mechanical properties of M270-35A steel used in the simulation are given in Table VII. The material has a yield strength of 365 MPa according to the datasheet. Linear material properties are assumed in the simulation, meaning that the plasticity of the material is neglected. The contacts between the magnets and the electrical steel are assumed to be frictionless, which shows the worst-case scenario.

TABLE VII MECHANICAL PROPERTIES OF M270-35A STEEL

Parameter	Value
Density (g/cm^3)	7.68
Young modulus (GPa)	200
Tensile strength (MPa)	490
Yield strength (MPa)	365
Elongation at break (%)	25

The equivalent Von Mises stress results of the mechanical simulation are presented in Fig. 20. It can be seen that the stress experienced by the bridges and the centre posts is less than the yield stress of the material at 20% overspeed conditions. The asymmetric nature of the proposed machines resulted in asymmetric stress distribution across the rotor body. The results show the proposed machines' mechanical validity.

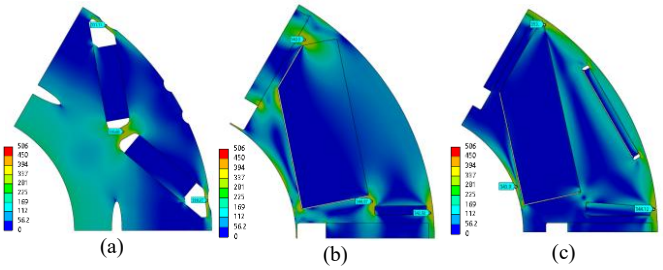

Fig. 20. Von-Mises stress in MPa distribution of machines at 20% overspeed conditions. (a) Reference, (b) Spoke-V, (c) Spoke-Delta.

C. *Torque-Speed Characteristic Analysis*

The proposed machine designs, along with the reference machine, are evaluated over the full operational speed range to assess their performance under realistic drive conditions. The reference design is specified to operate up to a maximum speed of 18000 r/min. The inverter is assumed to have a peak phase current capability of 1100 A, while the battery voltage is set at 350 V, consistent with typical electric vehicle drivetrain specifications. The analysis assumes the use of maximum torque per ampere (MTPA) control in the constant torque region and space vector pulse width modulation (SVPWM) in the inverter operation. These control strategies are commonly employed in high-performance electric drives to optimize torque output and voltage utilization across the speed range. Under these conditions, the machines are simulated to generate torque-speed characteristics, as well as detailed loss and efficiency maps. Mechanical losses are neglected in this comparison. The resultant torque speed and power speed curves are presented in Fig. 21. The results show that while the proposed machines have good enough performance at constant torque region, at high power regions there is a slight difference in the torque and power output.

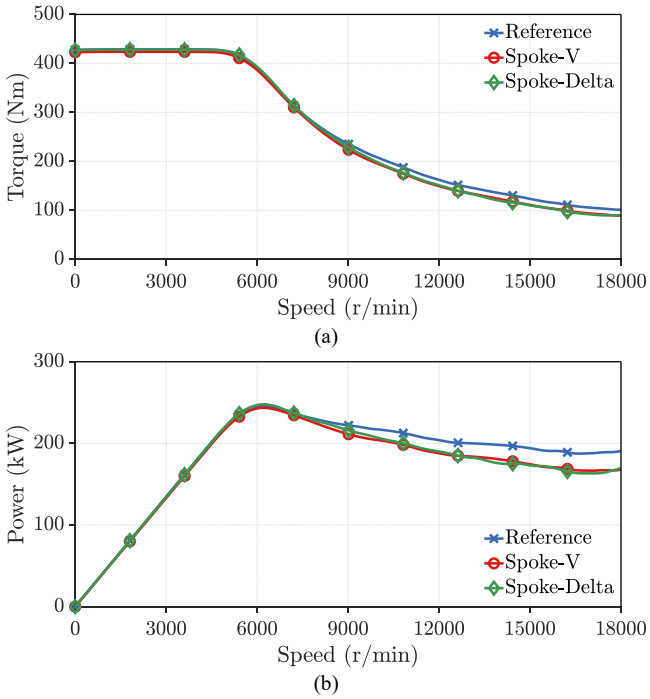

Fig. 21. Output torque and power speed curves. (a) Torque vs speed, (b) Power vs speed.

The copper loss, core loss, and resultant efficiency maps are shown in Fig. 22, Fig. 23, Fig. 24, respectively. The copper loss maps of the reference and the proposed machines are similar to each other since the machines are designed to have the same maximum copper loss value due to thermal limitations. The core loss maps indicate that spoke-delta machine has slightly lower core loss at higher speeds since the magnetic loading and back-EMF of this machine is lower than the other designs. The efficiency maps reveal a similar trend for the spoke-Delta machine at high-speed operation, whereas across the remaining operating regions the efficiency distributions of all machines exhibit largely comparable characteristics. The proposed spoke-V and spoke-delta designs exhibit broadly similar flux-weakening capability and high-speed efficiency. Both topologies are able to maintain effective flux reduction under negative *d*-axis current injection. At high speeds, their efficiencies remain comparable, as the copper and core losses are of similar magnitude for both machines.

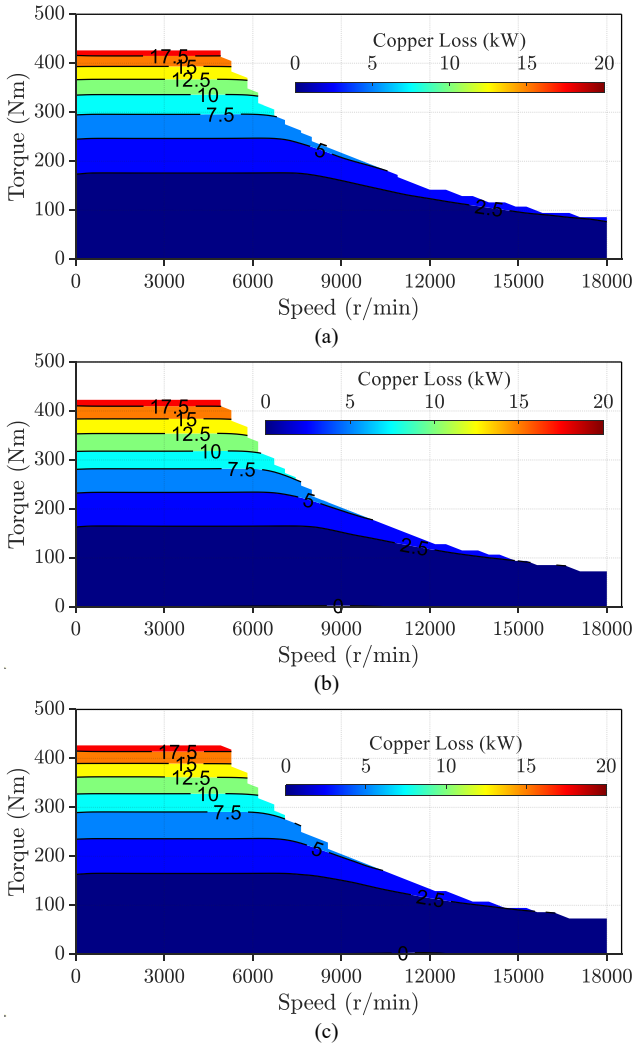

Fig. 22. Copper loss maps. (a) Reference, (b) Spoke-V, (c) Spoke-Delta.

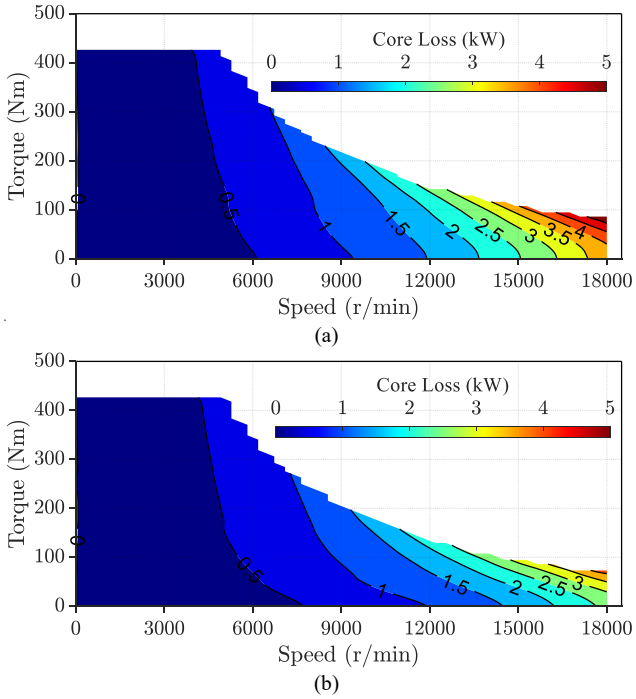

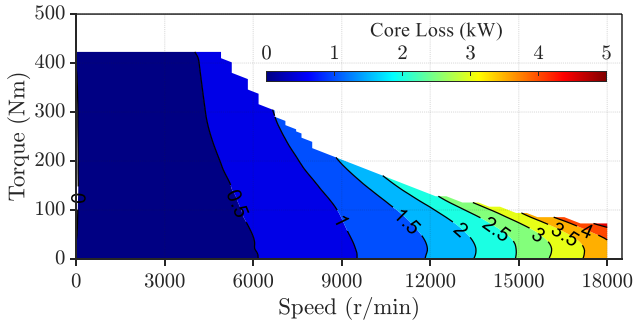

Fig. 23. Core loss maps. (a) Reference, (b) Spoke-V, (c) Spoke-Delta.

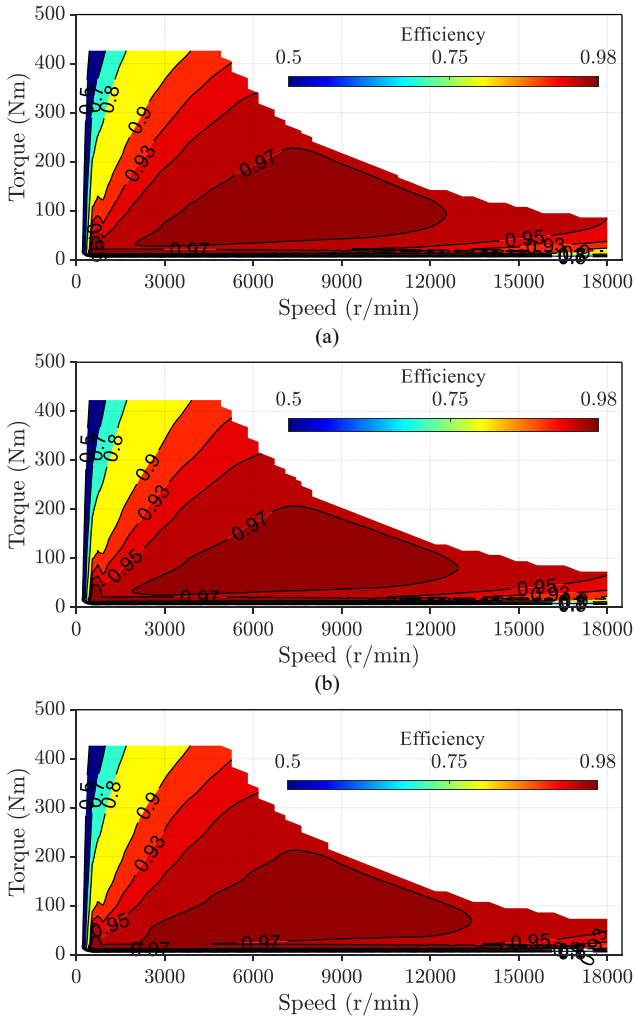

Fig. 24. Efficiency maps. (a) Reference, (b) Spoke-V, (c) Spoke-Delta.

V. Experimental Validation

To validate the simulation results, a small-scale prototype machine with a 24-slot/8-pole configuration is designed, manufactured, and tested. The 24-slot/8-pole configuration is selected due to its high winding factor and relative ease of manufacturability. A higher slot number, such as in the 54-slot layout, would make the fabrication and winding of a small-scale prototype more complex and costly. Since the prototype represents a scaled-down version of the proposed design, the relative contributions of magnet torque and reluctance torque differ from those of the full-scale machine. Specifically, reluctance torque is proportional to the square of the current,

whereas magnet torque scales directly with current. As a result, under the current density and dimensions employed in the prototype, the torque production is expected to be dominated by the PM torque component. The key design parameters for the prototype are provided in Table VIII. The machine uses both N42UH-grade NdFeB magnets and TDK-FB13B-grade ferrite magnets. Photos of the manufactured stator and rotor are shown in Fig. 25.

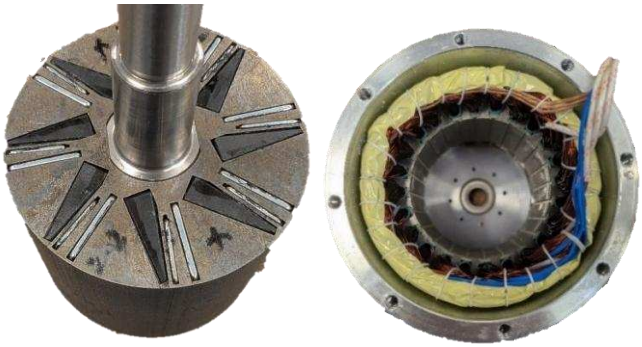

(a) (b)

Fig. 25. Asymmetric spoke-V rotor prototype. (a) Spoke-V rotor, (b) 24-slot stator.

TABLE VIII PARAMETERS OF PROTOTYPE MACHINE

Parameters	Value
Stator outer diameter (mm)	100
Stator inner diameter (mm)	63
Axial length (mm)	50
Number of stator slots	24
Number of poles	8
PM remanence (T)	1.31
Airgap (mm)	1
Maximum phase current (A)	4
Phase resistance (Ω)	1.6

The prototype is evaluated under a series of tests, beginning with static tests to measure cogging torque and static torque variation as a function of rotor position under constant DC excitation. The experimental setup used for these measurements is illustrated in Fig. 26. The cogging torque test is performed under open-circuit conditions with unenergized stator windings. The rotor is manually rotated in small increments over one cogging period, and the corresponding force is recorded using a weight scale. The torque is then calculated using the known lever arm length, following the method outlined in [29]. The comparison between FEA and experimental results for cogging torque, shown in Fig. 27, demonstrates good agreement.

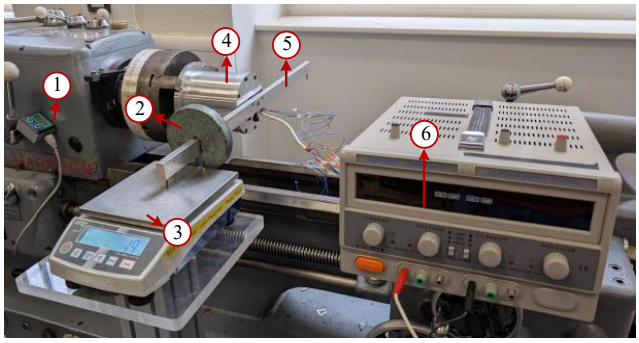

Fig. 26. Test setup for static testing. 1) Digital position sensor, 2) Weight, 3) Digital scale, 4) Prototype, 5) Balance beam, 6) Power supply.

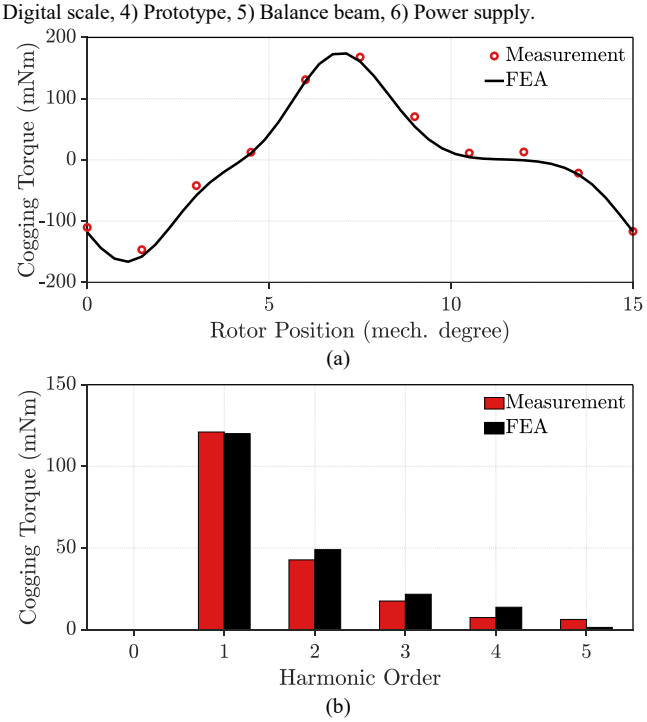

Fig. 27. FEA simulated and measured results of cogging torque. (a) Waveforms, (b) Spectra.

Static torque measurements are carried out using the same test rig. During the tests, a constant DC current is applied to the windings: 2 A to phase A, and -1 A to phases B and C. The rotor is rotated across one electrical period, and the resulting torque waveform along with its harmonic content is presented in Fig. 28. The deviation between measured and simulated torque values is less than 3.5%, confirming the accuracy of the simulation model. The accuracy of the results can be attributed to the precise modelling of the electrical steel and magnet properties in the FEA, as well as the high manufacturing accuracy of the prototype, which ensured close adherence to the designed geometry and winding configuration.

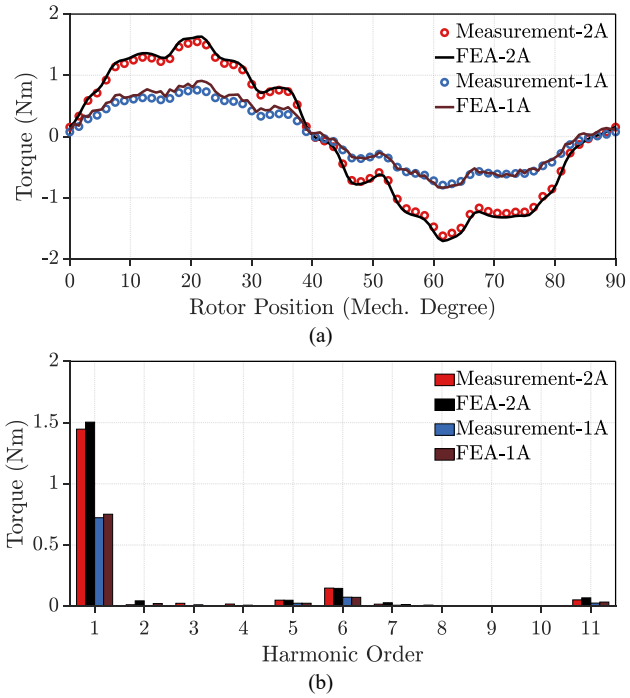

Fig. 28. Results of static torque in FEA and test at 1A and 2A of current. (a) Waveforms, (b) Spectra.

Dynamic performance is assessed using the setup shown in Fig. 29. The prototype is coupled with a torque transducer and a DC machine, with control implemented via a dSPACE interface. A position encoder mounted on the shaft provides real-time feedback for the control loop. Open-circuit test results at 750 r/min are presented in Fig. 30. The measured RMS value of the back-EMF is 45.19 V, closely matching the FEA prediction of 45.58 V, thereby validating the simulation accuracy. The results showed higher 11th and 13th harmonics in the back-EMF waveform which is not present in the simulated 54 slots/6 poles design. The difference is attributed to the chosen slot/pole number combination of the prototype which has different winding factor than the 54 slots/6 pole design. These high order harmonics are not expected to be increased in 54 slot/6 pole baseline design.

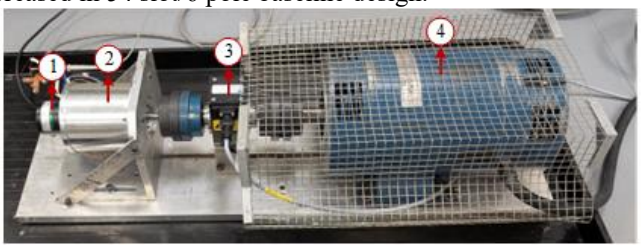

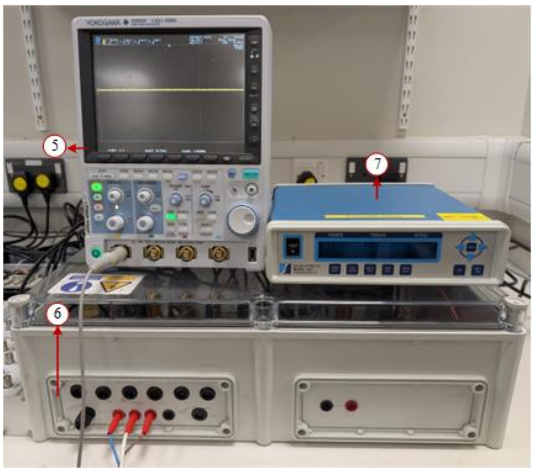

Fig. 29. Dynamic test setup. 1) Encoder, 2) Prototype, 3) Torque transducer, 4) DC machine, 5) Oscilloscope, 6) Inverter, 7) Torque display.

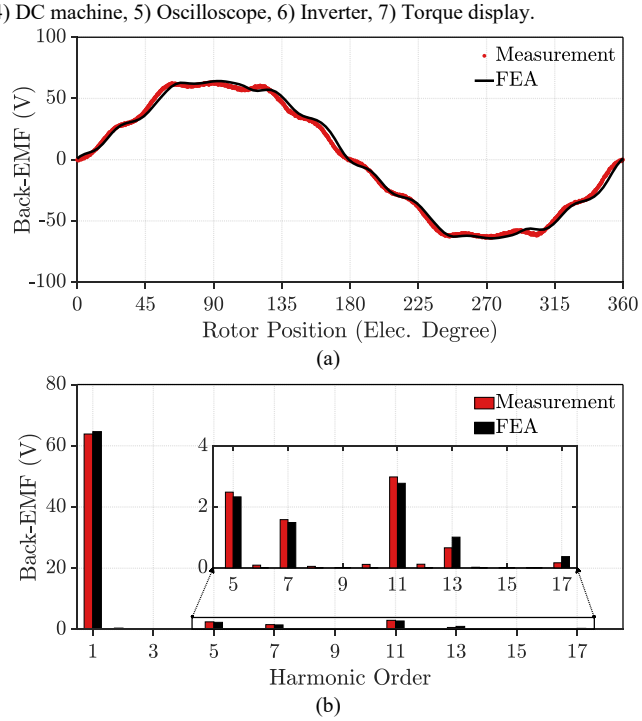

Fig. 30. Line back-EMFs at 750 r/min. (a) Waveforms, (b) Spectra.

Further testing is conducted under the loaded conditions. In this configuration, the DC machine operates as a generator and is connected to a resistive load bank. The prototype is driven by an inverter using SVPWM with a 65 V DC bus at 500 r/min. The change in average output torque with changing phase advance angle at 2 A of peak current is shown in Fig. 31. The machine peaks around 15 degrees phase advance angle with 1.51 Nm average torque. The results are also presented in table form in Table IX.

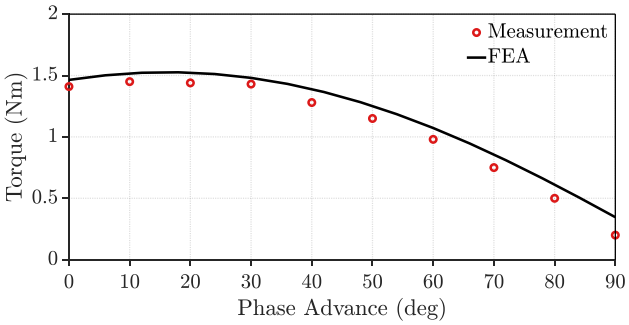

Fig. 31. Average torque change vs phase advance.

TABLE IX TORQUE AT DIFFERENT PHASE ADVANCE ANGLES

Phase Advance(deg)	0	10	20	30	40	50	60	70	80	90
FEA Torque (Nm)	1.46	1.49	1.50	1.48	1.37	1.23	1.07	0.82	0.55	0.34
Test Torque (Nm)	1.41	1.45	1.44	1.43	1.28	1.15	0.98	0.75	0.5	0.2

The average output torque as a function of phase current is depicted in Fig. 32. The maximum measured torque is 3.18 Nm in the forward direction and 3.05 Nm in the reverse, indicating a torque asymmetry of approximately 4%. This discrepancy is attributed to the reduced armature reaction typically observed in small-scale machines compared to full-scale systems.

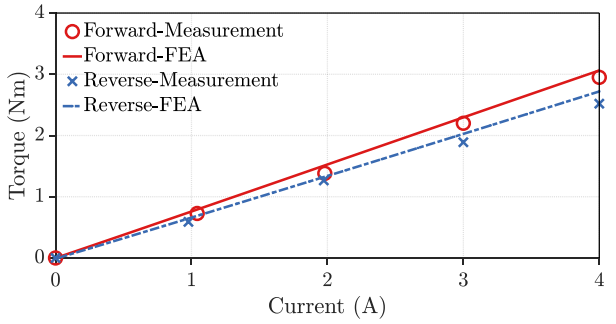

Fig. 32. Average torque change vs phase current in both rotational directions.

VI. CONCLUSION

This paper presents the design, optimization, and performance evaluation of two novel hybrid rotor topologies, spoke-V and spoke-delta, for high-speed IPMSMs for reducing rare-earth magnet usage without sacrificing electromagnetic performance. Using the Tesla Model 3 IPMSM as a reference, the proposed designs are optimized through a multi-objective NSGA-II algorithm to maximize average torque while minimizing the volume of NdFeB magnets. The spoke-V and spoke-delta designs have demonstrated up to 19.4% and 25.8% reductions in NdFeB magnet volume, respectively, while maintaining comparable torque output to the reference machine. These have translated to improvements of 20.5% and 35.1% in torque per unit volume of rare-earth material. The spoke-delta topology exhibits an increased saliency, and a magnetic field shift due to its asymmetric geometry, resulting in improved alignment between the PM and reluctance torque components and a shift in the optimal phase advance angle. Comprehensive evaluations under open-circuit, peak-load, and short-circuit conditions have confirmed the electromagnetic robustness of both designs. The proposed machines show the reduced torque ripple due to suppression of dominant harmonics and exhibit no signs of demagnetization. Efficiency and torque-speed analyses under full operating conditions have further validated their suitability for high-performance electric vehicle applications. Overall, the findings demonstrate that carefully engineered hybrid magnet rotor topologies with asymmetric features can significantly reduce rare-earth material dependence while preserving or enhancing key performance metrics. This contributes to the development of more sustainable, cost-effective electric machines and offers a promising design direction for future traction motor technologies.

REFERENCES

[1] T. Jahns, "Getting rare-earth magnets out of EV traction machines: A review of the many approaches being pursued to minimize or eliminate rare-earth magnets from future EV drivetrains," IEEE Electrification Magazine, vol. 5, no. 1, pp. 6-18, March 2017.
[2] Z.Q. Zhu, W.Q. Chu, and Y. Guan, "Quantitative comparison of electromagnetic performance of electrical machines for HEVs/EVs," CES Transactions on Electrical Machines and Systems, vol.1.no.1, pp.37-47, 2017.
[3] F. Tokgoz et al., "Feasibility analysis of multiphase machines for electric vehicle applications," IEEE Transactions on Industry Applications, vol. 61, no. 6, pp. 9216-9231, Nov.-Dec. 2025.
[4] F. Tokgoz, "Novel permanent magnet synchronous machines with reduced rare-earth magnets for electric Vehicles," Ph.D. dissertation, Electrical and Electronic Engineering, University of Sheffield., Sheffield, UK, Oct. 2025. Available : https://etheses.whiterose.ac.uk/id/eprint/37595
[5] B. Bilgin et al., "Making the case for electrified transportation," IEEE Transactions on Transportation Electrification, vol. 1, no. 1, pp. 4-17, June 2015.
[6] U.S. Geological Survey, 2024, Mineral commodity summaries 2024: U.S. Geological Survey, 212 p.
[7] D. G. Barroso, Y. Yang, F. A. Machado and A. Emadi, "Electrified automotive propulsion systems: State-of-the-art review," IEEE Transactions on Transportation Electrification, vol. 8, no. 2, pp. 2898-2914, June 2022.
[8] J. Cui et al., "Current progress and future challenges in rare-earth-free permanent magnets," Acta Materialia, vol. 158, pp. 118–137, Oct. 2018.
[9] J. Cui et al., "Manufacturing processes for permanent magnets: Part I-Sintering and casting," JOM, vol. 74, no. 4, pp. 1279–1295, Feb. 2022
[10] Y. Xie, J. Shao, S. He, B. Ye, F. Yang, and L. Wang, "Novel PM-assisted synchronous reluctance machines using asymmetrical rotor configuration," IEEE Access, vol. 10, pp. 79564–79573, Jan. 2022.
[11] B. Lv, L. Shi, L. Li, K. Liu, and J. Jing, "Performance analysis of asymmetrical less-rare-earth permanent magnet motor for electric vehicle," IET Electrical Systems in Transportation, vol. 12, no. 1, pp. 36–48, Sep. 2021.
[12] S. Kazemisangdehi, Z. Q. Zhu, Y. Zhou, H. Liu, L. Chen and L. Yang, "Novel parallel hybrid rare-Earth and ferrite Magnets in V-Spoke interior PM synchronous machine," IEEE Transactions on Industry Applications, vol. 61, no. 2, pp. 2972-2982, March-April 2025.
[13] Z. Q. Zhu and Y. Xiao, "Novel magnetic-field-shifting techniques in asymmetric rotor pole interior PM machines with enhanced torque density," IEEE Transactions on Magnetics, vol. 58, no. 2, pp. 1-10, Feb. 2022.
[14] F. Tokgoz et al., "Asymmetric and symmetrical rotor core shaping techniques of IPMSMs for EVs," 2023 26th International Conference on Electrical Machines and Systems (ICEMS), Zhuhai, China, 2023, pp. 377-382.
[15] F. Tokgoz et al., "Comparative study of multiphase IPMSMs for EV applications," 2023 26th International Conference on Electrical Machines and Systems (ICEMS), Zhuhai, China, 2023.
[16] R. Thike and P. Pillay, "Mathematical model of an interior PMSM with aligned magnet and reluctance torques," IEEE Transactions on Transportation Electrification, vol. 6, no. 2, pp. 647-658, June 2020.

[17]Y. Xiao et al., "A novel asymmetric interior permanent magnet machine for electric vehicles," IEEE Transactions on Energy Conversion, vol. 36, no. 3, pp. 2404-2415, Sept. 2021.
[18]Y. Xiao, Z. Q. Zhu, G. W. Jewell, J. Chen, D. Wu and L. Gong, "A novel spoke-type asymmetric rotor interior permanent magnet machine," IEEE Transactions on Industry Applications, vol. 57, no. 5, pp. 4840-4851, Sept.-Oct. 2021.
[19]M. Xu, G. Liu, Q. Chen, J. Ji and W. Zhao, "Torque calculation of stator modular PMa-SynRM with asymmetric design for electric vehicles," IEEE Transactions on Transportation Electrification, vol. 7, no. 1, pp. 202-213, March 2021.
[20]A. M. Ajamloo, A. Ghaheri, M. N. Ibrahim and P. Sergeant, "Investigation of different pole configurations in new asymmetric permanent magnet synchronous reluctance machines," IEEE Transactions on Magnetics, 2025.
[21]A. Mohammadi Ajamloo, A. Ghaheri, M. N. Ibrahim and P. Sergeant, "Principle of torque-axis alignment in new asymmetric PM synchronous reluctance machines: Toward less-rare-earth PM machines," IEEE Transactions on Transportation Electrification, vol. 11, no. 2, pp. 6392-6405, April 2025.
[22]W. Zhao, C. Diao, D. Chen, Y. Liu and X. Wang, "A permanent magnet concentrated-flux synchronous reluctance motor with torque improvement for unmanned ship propulsion," IEEE Transactions on Transportation Electrification, 2025.
[23]R. Tu et al., "A novel hybrid-pole variable flux memory machine with integrated series-parallel PM topology," IEEE Transactions on Transportation Electrification, vol. 11, no. 3, pp. 7577-7587, June 2025.
[24]W. Liu, H. Yang, H. Lin and Y. Zhong, "A novel three-stage optimization design method of asymmetric-PM variable flux memory machine considering magnet-axis-shifting effect," IEEE Transactions on Transportation Electrification, vol. 9, no. 1, pp. 336-346, March 2023.
[25]Y. Chen, T. Cai, X. Zhu, D. Fan and Q. Wang, "Analysis and design of a new type of less-rare-earth hybrid-magnet motor with different rotor topologies," IEEE Transactions on Applied Superconductivity, vol. 30, no. 4, pp. 1-6, June 2020.
[26]X. Zhu et al., "Torque component redistribution and enhancement for hybrid permanent magnet motor with permanent magnet offset placement," IEEE Transactions on Transportation Electrification, vol. 9, no. 1, pp. 631-641, March 2023.
[27]Y. Chen, X. Zhou, Z. Li and X. Zhu, "Torque performance enhancement for hybrid PM motor considering magnet characteristic difference and variation," IEEE Transactions on Magnetics, vol. 59, no. 11, pp. 1-5, Nov. 2023.
[28]S. Kazemisangdehi, Z. Q. Zhu, L. Chen, L. Yang and Y. Zhou, "A mixed hybrid rare-earth and ferrite magnet asymmetric V-shape IPMSM," IEEE Transactions on Transportation Electrification, 2025.
[29]Z. Q. Zhu, "A simple method for measuring cogging torque in permanent magnet machines," 2009 IEEE Power & Energy Society General Meeting, Calgary, AB, Canada, 2009.

Furkan Tokgoz (Member, IEEE) received the B.Sc. and M.Sc. degrees in Electrical-Electronics Engineering from the Middle East Technical University, Ankara, Turkey, in 2019 and 2022, respectively, and the Ph.D. degree in Electrical and Electronic Engineering from the University of Sheffield, Sheffield, U.K., in 2025, where he was a member of the Electrical Machines and Drives Group. He is currently with Monumo, Cambridge, U.K., where he focuses on AI-driven optimization of electric motor and drive systems. His research interests include electric machine design and optimization, axial-flux machines, PCB stator technology, and advanced motor drives for electric vehicle applications.

Z.Q. Zhu (Fellow, IEEE) (M'90, SM'00, F'09) received the B.Eng. and M.Sc. degrees from Zhejiang University, Hangzhou, China, in 1982 and 1984, respectively, and the Ph.D. degree from the University of Sheffield, Sheffield, U.K., in 1991, all in electrical engineering. From 1988 to 2025, he was with the University of Sheffield, as Professor (1997-2025), Royal Academy of Engineering/Siemens Research Chair (2014-2023), and Head of the Electrical Machines and Drives Research Group (2008-2025). Since 2025, he has been Chair Professor at the Hong Kong Polytechnic University. He is Founding Directors of several industrial research centers, including the Sheffield Siemens Gamesa Renewable Energy Research Centre and the Midea Shanghai Electric Machines and Control Systems Research Centre. His current major research interests include design and control of permanent magnet machines and drives for applications ranging from electrified transportation (electric vehicles, fast trains, electric aircrafts) to domestic appliances, industrial drives, robots, and automation components and systems. He is the recipient of the 2024 Global Energy Prize, the 2021 IEEE Nikola Tesla Award, and the 2019 IEEE IAS Outstanding Achievement Award. Prof. Zhu is a Fellow of Royal Academy of Engineering, U.K.; National Academy of Inventors, U.S.A.; Institute of Electrical and Electronics Engineers (IEEE), U.S.A.; Institute of Engineering and Technology (IET), U.K.; Chinese Society for Electrical Engineering (CSEE); and China Electrotechnical Society (CES).

Xiao Chen (M'16-SM'21) received BEng and MSc degrees in electrical engineering from Harbin Institute of Technology, China, in 2009 and 2011, respectively, and PhD degree in electrical machines from University of Sheffield, in 2015. He was a research associate at University of Sheffield, from 2016 to 2018, before working as an advanced motor drive engineer in Dyson, UK, until 2019. Then he rejoined University of Sheffield as a lectuer and has been a senior lectuer since 2024. His current research interests include bearing currents, high frequency effects in electrical machines, manufacturing impact on electrical machine performances, high-fidelity modelling of electrical machines, multi-physics effects in electrical machines, etc.

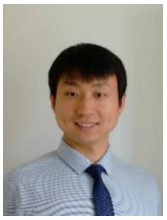

Chaohui Liu (M'14) received the B.E. from North University of China, M.E from Beihang University, and Ph.D. in the Electrical Machines and Drives (EMD) Research Group from the University of Sheffield, UK in 2006, 2011 and 2017 respectively. From 2017 to 2020, he was with the Department of Research, Design and Development, Dyson Technology Limited, UK, where he was appointed an Advanced Engineer in 2017 and Senior Engineer in 2018. He is currently a Principle Engineer and the Head of Powertrain at National New Energy Vehicle Technology Innovation Center (NEVC), Beijing, China. His research interests include machine drive, advanced control strategy, power converters, electric vehicle battery charger, wide band-gap device packaging and power module applications.

Lianghui Yang received Doctor of Engineering. He currently is the Deputy Director of NEVC Xiamen, responsible for Research & Development. Formerly the technical leader of the electric drive assembly department of a leading domestic new energy vehicle company, he has been engaged in the R&D of electric drive technology in new energy vehicles for 13 years. He has rich

experience in the development of the overall performance of new energy vehicles. He has presided over the vehicle development projects of many pure electric models and was responsible for the development of many new energy vehicle electric drive assemblies (with an application scale of more than 300,000 vehicles). He has been responsible for and participated in many scientific research projects of the Ministry of Science and Technology of China and the Beijing Municipal Science and Technology Commission and won the second prize of the industry science and technology award.

Yiqing Yuan is specially appointed expert of the National "Thousand Talents Plan", academician of the Russian Academy of Engineering, doctor of Virginia Polytechnic Institute and State University, Professor and doctoral supervisor of Tongji University. He participated in the demonstration, design, testing and improvement of various automatic transmissions of Chrysler. He is former deputy general manager of Zhongke Shenjiang, led the development of transmissions for electric vehicles, planned and formed the product series of reducers, 2-speed AMT, and electric continuously variable transmissions. From 2013 to now, he has been the chairman and general manager of Qiancheng Electronics Company, developing a series of 2-speed AMT products for electric vehicles.

Han Yang received Engineering PhD from the University of Sheffield, UK in 2019, was a research fellow at Warwick Manufacturing Group (WMG), UK. He is currently the head of the motor business at NEVC-Xiamen. He was previously the head of the R&D department of a leading motor manufacturing company in Xiamen, and the project manager of the mass production project of SAIC flat wire motors. He has extensive experience in the R&D and design of permanent magnet synchronous motors.

Yiming Huang is a Chief expert in semiconductor technology, an expert in integrated circuit standards of the Ministry of Industry and Information Technology, an expert in basic research in the field of aerospace science and technology innovation during the 13th Five-Year Plan. Former deputy chief engineer of the 13th Institute of China Electronics Technology Group; Vice President of NeoPhotonics Corp. He has undertaken more than 20 projects including the National Natural Science Foundation, the 863 Program, the "National Major Science and Technology Project of Nuclear High-tech, independent Scientific Research, innovation Fund, FIT Fund, etc. He published more than 100 papers in journals such as IEEE TPDS and IEEE TVLSI and international conferences, authorized 10 invention patents, formulated 1 industry standard and 10 national standards, and 2 books.